Ni-based transition metal trichalcogenide monolayer: A strongly correlated quadruple-layer graphene

Yuhao Gu,[1,2] Qiang Zhang,[2] Congcong Le,[3,2] Yinxiang Li,[2] Tao Xiang,[2,3,4] and Jiangping Hu[2,3,4,*]

[1]*Beijing National Laboratory for Molecular Sciences, State Key Laboratory of Rare Earth Materials Chemistry and Applications, Institute of Theoretical and Computational Chemistry, College of Chemistry and Molecular Engineering, Peking University, 100871 Beijing, China*

[2]*Beijing National Laboratory for Condensed Matter Physics, and Institute of Physics, Chinese Academy of Sciences, Beijing 100190, China*

[3]*Kavli Institute of Theoretical Sciences, University of Chinese Academy of Sciences, Beijing, 100190, China*

[4]*Collaborative Innovation Center of Quantum Matter, Beijing, China*

(Received 14 November 2018; revised manuscript received 8 September 2019; published 4 October 2019)

We investigate the electronic physics of layered Ni-based trichalcogenide $NiPX_3$ (X = S, Se), a member of transition metal trichalcogenides (TMTs) with the chemical formula ABX_3. These Ni-based TMTs distinguish themselves from other TMTs as their low energy electronic physics can be effectively described by the two e_g d orbitals. The major band kinematics is characterized by the unusual long-range effective hopping between two third nearest-neighbor (TNN) Ni sites in the two-dimensional Ni honeycomb lattice so that the Ni lattice can be equivalently viewed as four weakly coupled honeycomb sublattices. Within each sublattice, the electronic physics is described by a strongly correlated two-orbital graphene-type model that results in an antiferromagnetic (AFM) ground state near half-filling. We show that the low energy physics in a paramagnetic state is determined by the eight Dirac cones which locate at K, K', $\frac{K}{2}$, and $\frac{K'}{2}$ points in the first Brillouin zone with a strong AFM fluctuation between two K (K') and $\frac{K'}{2}$ ($\frac{K}{2}$) Dirac cones and carrier doping can sufficiently suppress the long-range AFM order and allow other competing orders, such as superconductivity, to emerge. The material can be an ideal system to study many exotic phenomena emerged from strong electron-electron correlation, including a potential $d \pm id$ superconducting state at high temperature.

DOI: 10.1103/PhysRevB.100.165405

I. INTRODUCTION

Since the discovery of graphene [1] a decade ago, two-dimensional (2D) materials have been a research frontier for both fundamental physics and practical device applications [2,3]. Transition metal trichalcogenides (TMTs) with the chemical formula ABX_3 (X = S, Se, Te), which were known more than a century ago [4,5], are layered van der Waals (vdW) materials. Recently, this family of materials has attracted great research attention as potential excellent candidates to explore 2D magnetism for novel spintronics applications.

All the members in the family of ABX_3 materials are built on a common structural unit, $(P_2X_6)^{4-}$ (X=S, Se, Te) anion complex. However, the cation atom A is rather flexible, ranging from vanadium to zinc (A = V, Cr, Mn, Fe, Co, Ni, Zn, etc.) in the row of the 3d transition metal, partial alkaline metal in group-II, and some other metal ions. As shown in Figs. 1(a) and 1(b), the cation is coordinated with six chalcogen anions to form an octahedra complex. In the two-dimensional layer, the cation forms a graphene-type honeycomb lattice. The transition metal trichalcogenides exhibit a variety of intriguing magnetically ordered insulating states [6]. Recently, under high pressure, $FePSe_3$ can also become a superconductor [7].

Among this family of materials, the Ni-based trichalcogenides can carry intriguing electronic physics, such as strong charge-spin coupling [8], because of the following reasons. First, as the transition metal cation and chalcogen anions form an octahedral complex, the 3d orbitals of the transition metal are divided into high energy e_g and low energy t_{2g} groups. In the case for Ni which has eight electrons in the 3d shell, the t_{2g} orbitals are fully occupied and the two e_g orbitals are half-filled as shown in Fig. 1(c). The t_{2g} orbitals are inactive. The Ni-based trichalcogenides should be described by a relatively simpler low energy effective model than other materials. Second, unlike a two-dimensional square lattice, a honeycomb lattice easily exhibits a Dirac-cone type of energy dispersion [9]. Near half-filling, both a one-orbital model, such as graphene [1], and two-orbital models [10,11] in the honeycomb lattice are featured with Dirac points near Fermi energy. With the strong electron-electron correlation in the 3d orbitals, the Ni-based trichalcogenide thus can be a candidate of strongly correlated Dirac electron systems. It is worth mentioning that a recent major research effort has aimed to increase the electron-electron correlation in graphene [12], in which flat bands have to be engineered to observe correlation effects because of p orbitals. Finally, both density functional theory (DFT) calculation and experimental measurements have suggested that the Ni honeycomb lattice forms the zigzag antiferromagnetic insulating ground state featured as double parallel ferromagnetic chains being antiferromagnetically (AFM) coupled [6,13]. The material offers a promising platform to study the interplay between the low energy Dirac electronic physics and the magnetism. Such an interplay is believed to be responsible for many important

*jphu@iphy.ac.cn

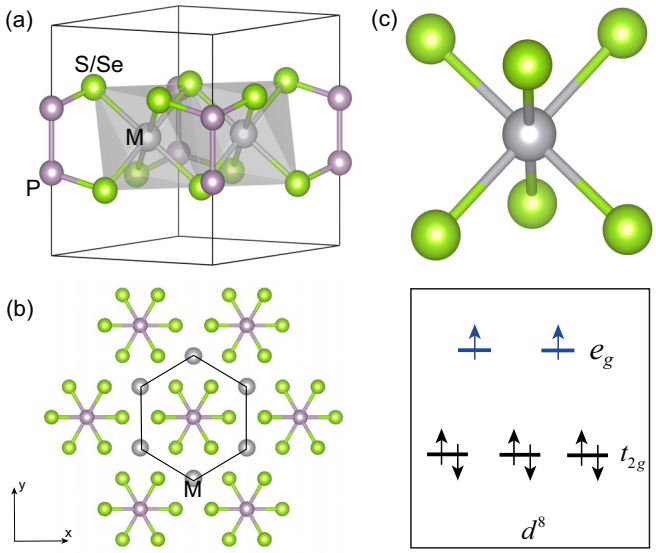

FIG. 1. (a) The crystal structures of the monolayer $NiPX_3$ (X = S, Se) (space group $P-31m$). (b) The top view of the monolayer $NiPX_3$. (c) The octahedral crystal field splitting of Ni atoms.

phenomena, for example, high temperature superconductivity in both cuprates and iron-based superconductors [14,15].

In this paper we show that the Ni-based TMTs are Dirac materials with strong electron-electron correlation. Their low energy electronic physics can be entirely attributed to the two e_g d orbitals with a band kinematics dominated by the unusual "long-range" hoppings between two third nearest-neighbor (TNN) Ni sites in the Ni honeycomb lattice. Thus, the original Ni lattice can be divided into four weakly coupled honeycomb sublattices. Within each sublattice, the electronic physics is described by a strongly correlated two-orbital graphene-type model. The couplings between four sublattices, namely, the nearest-neighbor (NN) and the second NN (SNN) hoppings in the original lattice, can be adjusted by applying external pressure or chemical methods. In the absence of the strong electron-electron correlation, the low energy physics is determined by the eight Dirac cones which locate at K (K') and three nonequivalent pairs of $\frac{K}{2}$ ($\frac{K'}{2}$) points in the first Brillouin zone. In the presence of strong electron-electron correlation, strong AFM interactions arise between two NN sites within each honeycomb sublattice. Namely, in view of the original honeycomb lattice, the strong AFM interactions only exist between two TNN sites. Near half-filling, Dirac cones are gapped out by the long-range AFM order. Using the standard slave-boson approach, we show that the doping can sufficiently suppress the long-range AFM order. In a wide range of doping, a strong AFM fluctuation can exist between the Dirac cones and a $d \pm id$ superconducting state can be developed.

It is interesting to make an analogy between the above results and those known in high temperature superconductors, cuprates, and iron-based superconductors. For the latter, it is known that the dominant AFM interactions are between two NN sites in cuprates and between two SNN sites in iron-based superconductors, which are believed to be responsible for the d-wave and the extended s-wave pairing superconducting states, respectively [14–16]. All these AFM interactions are generated through superexchange mechanism. Thus, the Ni-based TMTs, having the AFM interactions between two TNN sites, can potentially provide the ultimate piece of evidence to settle superconducting mechanism in unconventional high temperature superconductors.

This paper is organized as follows. In Sec. II we briefly review transition metal phosphorous trichalcogenides and specify our DFT computation methods for magnetism and band structures. In Sec. III we analyze the band structure of the paramagnetic states, derive the tight-binding Hamiltonian, and discuss the low energy physics near Fermi surfaces. In Sec. IV we calculate the magnetic states of the materials and derive the effective magnetic exchange coupling parameters. In Sec. V we use the slave-boson mean-field method to derive the phase diagram upon doping and discuss the possible superconducting states. In the last section, we make summary and discussion.

II. TRANSITION METAL PHOSPHOROUS TRICHALCOGENIDES

The MPX_3 metal phosphorous trichalcogenides (M = Mg, Sn, Sc, Mn, Fe, Co, Ni, Cd, etc. and X = S, Se) are a famous family of 2D van der Waals (vdW) materials [2,3]. The bulk MPX_3 crystal consists of AA-stacked or ABC-stacked single-layer assemblies which are held together by the vdW interaction. The vdW gap distance of the MPX_3 with $3d$ transition metal elements is about 3.2 Å, much wider than the well studied MoS_2-type 2D vdW materials [17], which indicates that the vdW interaction in MPX_3 is relatively weak. The monolayer structure of MPX_3 is constructed by MX_6 edge shared octahedral complexes. Similar to the MoS_2-type MX_2 materials, the monolayer MPX_3 can be considered as the monolayer MX_2 with one third of M sites substituted by P_2 dimers, i.e., MPX_3 can be considered as $M_{2/3}(P2)_{1/3}X_2$. Thus, the triangle lattice in MX_2 transforms to the honeycomb lattice in MPX_3 with the $P_2X_6^{4-}$ anions being located at the center of the honeycomb. The P-P and P-X bond lengths indicate that the P-P and P-X bonds are covalent bonds in $P_2X_6^{2-}$ anions. As the transition metal atoms are in an octahedral environment, the five d orbitals are split into two groups, e_g and t_{2g}, as shown Fig. 1(c).

With the weak vdW interaction, the essential electronic physics in MPX_3 is determined within a monolayer. In fact, the atomically thin $FePS_3$ layer has been experimentally synthesized [18]. In this paper we mainly study the electronic physics in the monolayer MPX_3 structures. Without further specification, our study and calculations are performed in the monolayer structures as shown in Figs. 1(a) and 1(b).

Our DFT calculation is performed for the monolayer MPX_3 structures together with built-in 20 Å thick vacuum layers. We employ the Vienna *ab initio* simulation package (VASP) code [23] with the projector augmented wave (PAW) method [24] to perform the DFT calculations. The Perdew-Burke-Ernzerhof (PBE) [25] exchange-correlation functional was used in our calculations. Throughout this work, the kinetic energy cutoff (ENCUT) is set to be 500 eV for expanding the wave functions into a plane-wave basis and the Γ-centered k mesh is $16 \times 16 \times 1$ for the nonmagnetic unit cell.

TABLE I. The optimized and experimental structural parameters for MPX_3 (space group $P-31m$). The optimized results are in the lowest energy magnetic states. The AFM-zigzag/stripy order slightly breaks hexagonal symmetry.

System	a (Å)	M-X (Å)	P-X (Å)	P-P (Å)	M-X-M (deg)
$MnPS_3$, opt (AFM-Neel)	6.05	2.60	2.04	2.21	84.3
$MnPS_3$, exp [19]	6.08	2.63	2.03	2.19	83.9
$FePS_3$, opt (AFM-zigzag)	5.87/5.94	2.47/2.51/2.56	2.04/2.05	2.20	83.2/90.6
$FePS_3$, exp [19]	5.94	2.55	2.02	2.19	84.7
$CoPS_3$, opt (AFM-stripy)	5.77	2.34	2.08/2.09	2.19	90.8/90.9
$CoPS_3$, exp [20]	5.91	2.51	2.04	2.17	85.5
$NiPS_3$, opt (AFM-zigzag)	5.82	2.44	2.05	2.18	87.1/87.2
$NiPS_3$, exp [21]	5.82	2.50	1.98	2.17	84.4
$NiPSe_3$, opt (AFM-zigzag)	6.17	2.54	3.45/3.46	2.22	89.1/89.4
$NiPSe_3$, exp[22]	6.13	2.61	2.09	2.24	85.2

The energy convergence criterion is 10^{-6} eV. All structures are fully relaxed while forces are minimized to less than 0.01 eV/Å with the lowest energy magnetic states. The optimized and experimental structural parameters of the MPX_3 are listed in Table I. In the study of an effective Hamiltonian, we employ Wannier90 [26] to calculate the hopping parameters of the tight-binding model. In the study of magnetism of MPX_3, the GGA plus on-site repulsion U method (GGA+U) in the formulation of Liechtenstein *et al.* [27] is employed to describe the associated electron-electron correlation effect. The effective Hubbard U (U_{eff}) is defined by $U_{\text{eff}} = U - J_{\text{Hund}}$. In order to describe different magnetic orders, we build $2 \times 1 \times 1$ supercell and the k mesh is $8 \times 16 \times 1$, correspondingly.

III. ELECTRONIC BAND STRUCTURES AND THE TIGHT-BINDING MODEL FOR Ni-TRICHALCOGENIDES

In Fig. 2 we plot the band structures of $NiPS_3$ and $NiPSe_3$, which are similar to each other. From Fig. 2 it is clear that the five d-orbital bands are divided into two groups separated by a large crystal field splitting energy. The groups at the high and low energy are attributed to the two e_g and three t_{2g} orbitals, respectively. The bands from t_{2g} orbitals are completely filled while the four bands from the two e_g orbitals are close to half-filling. This is consistent with the fact that the Ni^{2+} cations are six-coordinated with an octahedral geometry and the d^8 configuration in Ni^{2+} contributes two electrons to the two e_g orbitals. The physics near Fermi energy is controlled by the two e_g $d_{xz/yz}$ orbitals. It is also worth noting that the contribution of the S/Se-p orbitals is considerable, especially near Γ point, which indicates strong d-p hybridization. As shown in Fig. 2, d-p hybridization is stronger in $NiPSe_3$ than in $NiPS_3$.

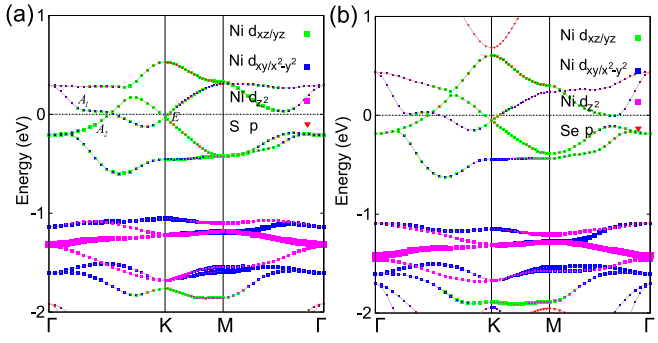

FIG. 2. Electronic band structures of (a) $NiPS_3$ and (b) $NiPSe_3$. The orbital characters of bands are represented by different colors.

Similar to the single orbital band structure in graphene, the two e_g orbital bands are featured by Dirac points as well. Here, there are eight Dirac points which locate at K and K' points, as well as around $K/2$ and $K'/2$ points along Γ-K line as shown in Fig. 2. These Dirac points are rather robust. To show the robustness, we analyze the symmetric character of the bands, namely, their irreducible representations. The two crossing bands along Γ-K line belong to A_1 and A_2 irreducible representations, and the bands at K points belong to E irreducible representation. Thus, the Dirac points are protected by the symmetry as the bands belong to different representations.

In order to capture the two-dimensional electronic physics near the Fermi level, we construct the tight-binding Hamiltonian based on the two e_g orbitals. The Hamiltonian can be written as

$$H_0 = \sum_k \psi_k^\dagger h_k \psi_k, \tag{1}$$

where the basis $\psi_k^\dagger = (a_{xk}^\dagger, a_{yk}^\dagger, b_{xk}^\dagger, b_{yk}^\dagger)$ and

$$h_k = \begin{pmatrix} \omega_k - \mu & \gamma_k \\ \gamma_k^\dagger & \omega_k^T - \mu \end{pmatrix}, \tag{2}$$

with μ being the chemical potential and

$$\omega_k = \sum_j e^{-i\mathbf{k}\cdot\mathbf{a_{2j}}} T_j^{\text{SNN}}, \tag{3}$$

$$\gamma_k = \sum_j e^{-i\mathbf{k}\cdot\mathbf{a_{1j}}} T_j^{\text{NN}} + e^{-i\mathbf{k}\cdot\mathbf{a_{3j}}} T_j^{\text{TNN}}. \tag{4}$$

Here $a_{xk}^\dagger$ ($b_{yk}^\dagger$) is the electron annihilator operator of orbital xz (yz) in the usual A (B) sublattice of the honeycomb lattice and vectors $\mathbf{a_1}$, $\mathbf{a_2}$, $\mathbf{a_3}$ are the first, second, and third neighbor vectors. $T_j^i = C_{3j} T^i C_{3j}^{-1}$ is the ith neighbor hopping matrix via the bond along ij bond direction, and C_{3j} is the threefold rotation operation to the ij direction relative to the initial setting. $T^i (i = \text{NN, SNN, TNN})$ is the hopping matrix with

TABLE II. The NN, SNN, and TNN hopping parameters and the bandwidths for $NiPS_3$ and $NiPSe_3$; xz and yz represent the band indexes of the hopping parameters. The bandwidths are from DFT results.

	$NiPS_3$	$NiPSe_3$
t^{NN}_{xzxz} (eV)	−0.054936	−0.059669
t^{NN}_{yzyz} (eV)	−0.026945	−0.001719
t^{SNN}_{xzxz} (eV)	0.020904	0.034843
t^{SNN}_{yzyz} (eV)	−0.017221	−0.017351
t^{SNN}_{xzyz} (eV)	0.006165	0.014114
t^{TNN}_{xzxz} (eV)	−0.017912	−0.021366
t^{TNN}_{yzyz} (eV)	0.232421	0.218275
e_g bandwidth (eV)	1.13	1.23

the direction marked in Fig. 3(a):

$$T^i = \begin{pmatrix} t^i_{xzxz} & t^i_{xzyz} \\ -t^{i*}_{xzyz} & t^i_{yzyz} \end{pmatrix}. \quad (5)$$

By the lattice symmetry, $t^{NN}_{xzyz} = t^{TNN}_{xzyz} = 0$. We will use eV as the energy unit for all hopping parameters. The results of $NiPS_3$ and $NiPSe_3$ are similar, as shown in Table II. The explicit formula of the Hamiltonian is given in Appendix A. Here we focus on the results of $NiPS_3$.

It is interesting to notice that the leading term in the above Hamiltonian is t^{TNN}_{yzyz}, the TNN σ-bond hoppings as shown in Fig. 3(a), which is almost one order of magnitude larger than the other hopping parameters, namely, the NN and SNN hopping parameters. Thus, we can consider these TNN hoppings as the dominant hopping parameters and treat other hoppings as perturbations. In Fig. 4(a) we plot the band dispersion with only the TNN hopping parameters. With only these TNN hoppings, the original Ni honeycomb lattice is divided into four decoupled sublattices as shown in Fig. 3(b). Within each honeycomb sublattice, the model is identical to the one previously studied in an ultracold atomic honeycomb lattice with two degenerate p orbitals [10,11]. As shown in Fig. 4(a), there are two completely flat bands and two dispersive bands. The flat bands stem from the localized binding and antibinding molecular orbitals [10]. The two dispersive

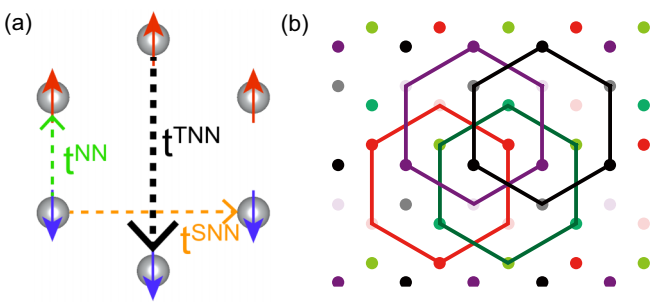

FIG. 3. (a) The three NN, SNN, and TNN hopping parameters marked by the green, brown, and black dashed arrows, respectively, and the zigzag AFM order with on-site red/blue arrows indicating spin up/down. (b) The four honeycomb sublattices.

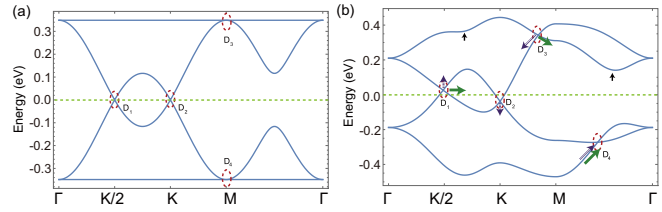

FIG. 4. The effect of different hopping parameters on the band structure and Dirac points. (a) The band dispersion with only the leading TNN hopping t^{TNN}_{yzyz}. (b) The band dispersion with all hopping parameters: the green, purple, and black arrows represent the motion of the band and Dirac points by increasing the NN, SNN, and TNN hopping parameters, respectively.

bands create the eight Dirac points. With only these TNN hoppings, the second pair of Dirac points are exactly located at $K/2$ and $K'/2$ points. This pair is simply created through the Brillouin zone folding because of the sublattice structure. Thus, the presence of the two pairs of Dirac points underlines the sublattice structure.

The dominance of the t^{TNN}_{yzyz} in $NiPX_3$ can be understood from the lattice chemistry. The Ni-e_g orbitals are strongly coupled with S/Se-p orbitals. These effective hoppings are mediated through the central $P_2X_6^{4-}$ anion. For the NN hoppings, two NN Ni atoms are in two edge shared MX_6 octahedral complexes. As the Ni-X-Ni angle is close to 90°, the NN indirect hopping through X is very small. The SNN effective hopping is mediated by two S/Se atoms which separately locate in the top and bottom layers. The coupling between these two S/Se atoms is weak due to the long distance around 3.8 Å between them, which explains the weak SNN hoppings. By contrast, the TNN σ hopping parameter is mediated through two S/Se atoms in the same layer.

The effects of other hopping parameters on Dirac points and band structures are indicated in Fig. 4(b), in which the arrows represent the motion of Dirac points and band structures when the corresponding hopping parameters increase. More specifically, the weak third neighbor π-bond hoppings t^{TNN}_{xzxz} neither affect the Dirac cones at K and $K/2$, nor the band degeneracy points at Γ and M. They only affect the flat bands in Fig. 4(a) far away from Fermi energy. The flat bands turn to disperse when t^{TNN}_{xzxz} increases. Therefore, in the weak hopping region, the low energy physics near Fermi surfaces are not affected by the third neighbor π-bond hoppings. The weak second nearest-neighbor hoppings, t^{SNN}_{xzxz} and t^{SNN}_{yzyz}, shift the Dirac points at $K/2$ and K vertically. By increasing these hoppings, the two Dirac points shift in opposite directions by a shift ratio equal to 3 as indicated by the purple arrows in Fig. 4(b). The weak NN hoppings t^{NN}_{xzxz} and t^{NN}_{yzyz} do not affect the Dirac cone at K because of the symmetry protection from the C_3, time reversal, and inversion symmetries. However, it drags the $K/2$ Dirac cone along Γ-K line as indicated by the green arrows in Fig. 4(b). Band crossing points D_3 and D_4 are also dragged along the direction indicated by the green arrows in Fig. 4(b).

The Fermi surfaces at the different doping levels are shown in Fig. 5. Without the SNN hoppings, the model gives Dirac semimetals at half-filling. Thus, the tiny pockets at half-filling shown in Fig. 5 stem from very small SNN hoppings. Due to

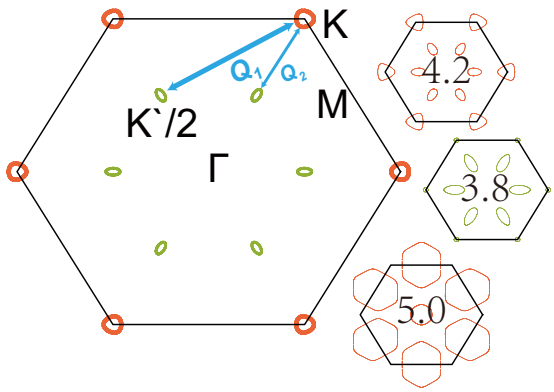

FIG. 5. Fermi surfaces and nesting vectors. The electron pockets and hole pockets are marked by red and green, respectively. The insets from top to bottom are Fermi surfaces at three doping levels, 0.1 (electron), −0.1 (hole), and 0.5 (electron) per Ni atom with respect to the half-filling, corresponding to formula $x = (n-4)/2$ with n the total electrons in each unit cell. In (a), nesting vectors $\mathbf{Q}_1$ and $\mathbf{Q}_2$ are depicted.

charge conservation, the area of electron pockets at $K/2$ are three times smaller than those hole pockets at K. In principle, with very small hole doping, strong nesting can take place between the electron and hole pockets at K and $K'/2$, respectively, but not at K and $K/2$, by taking into consideration of the shapes of Fermi pockets. By increasing hole (electron) doping, both pockets at K and $K/2$ become hole (electron) pockets. When the doping reaches around 0.3 carriers per Ni atoms, there is a Lifshitz transition of Fermi surfaces, namely, the two pockets emerging together to become one Fermi surface.

From the above Fermi surface topology, we can consider the possible Fermi surface nesting in a paramagnetic state. Near half-filling, the nesting vector is given by $\mathbf{Q}_1 = \mathbf{G}/2$, half of the reciprocal lattice vector, as highlighted in Fig. 5. This vector is exactly the ordered magnetic wave vector in the AFM zigzag state. We calculate the spin susceptibility under random phase approximation (RPA), with the same method and notations specified in literature [28,29]. The result is plotted in Fig. 6 for several different doping levels. Clearly the susceptibility peak emerges at M ($\mathbf{Q}_1$) near half-filling. Below the critical doping at the Lifshitz transition, the peak is well preserved, indicating the existence of strong AFM fluctuations. For a two-dimensional honeycomb lattice with hexagonal symmetry, there are six type-II van Hove (VH) saddle points near $K/2$ at the doping level of 0.35 electron per Ni atom. These type II VH singularities with an insufficiently nested Fermi surface (FS) result in the divergence of spin susceptibility at Gamma point, as shown in Fig. 6(d). Generally, doping close to type-II VH singularity, triplet pairing could compete with singlet pairing in the system [30].

IV. MAGNETIC EXCHANGE COUPLING PARAMETERS AND THE AFM ZIGZAG STATE

Without doping, MPX_3 are known to be magnetic insulators [2,3,13,31]. As the magnetic moments are localized at the transition metal atoms, the magnetism can be captured by an effective Heisenberg model with local magnetic moments.

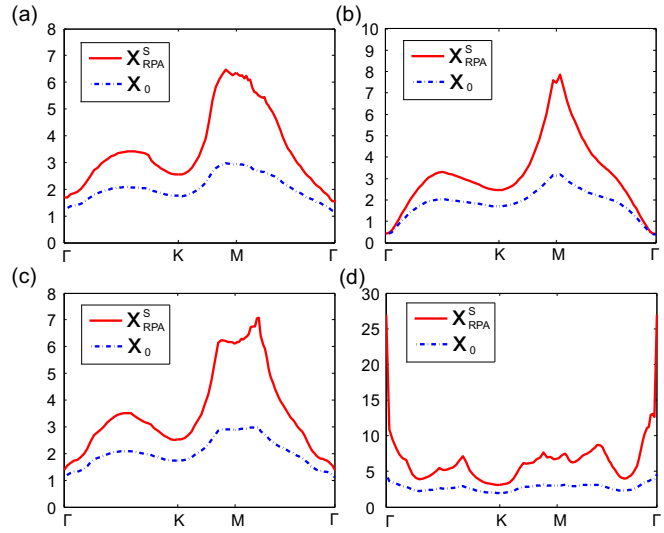

FIG. 6. Bare (dashed blue line) and RPA (solid red line) spin susceptibility for different doping levels: (a) half-filling, (b) 0.1, (c) −0.1, and (d) 0.35 (Liftshiz point where K and $K/2$ pockets connect). Here the on-site energy $U = 0.3$ eV and Hund's coupling $J_h = 0.2U$ is adopted, similar to Ref. [28]. Resonance apexes appear around the nesting vector $\mathbf{Q}_1$ (M) and $\mathbf{Q}_2$ ($K/2$) marked in Fig. 5.

As the effect of the spin-orbital coupling is generally small for e_g orbitals, we expect an isotropic Heisenberg model. Furthermore, from the lattice structure, it is obvious that the minimum effective model should include NN, SNN, and TNN magnetic exchange coupling parameters. Namely, the model can be written as

$$H = J_1 \sum_{\langle ij\rangle_{\mathrm{NN}}} \vec{S}_i \cdot \vec{S}_j + J_2 \sum_{\langle ij\rangle_{\mathrm{SNN}}} \vec{S}_i \cdot \vec{S}_j + J_3 \sum_{\langle ij\rangle_{\mathrm{TNN}}} \vec{S}_i \cdot \vec{S}_j. \quad (6)$$

To extract the magnetic exchange coupling parameters, we consider the following four different magnetic states: the ferromagnetic (FM) state, the AFM Neel state, the AFM zigzag, and the AFM stripy for MPS_3 (M = Mn, Fe, Co, Ni) which have been synthesized experimentally. Those four magnetic ordering arrangements are shown in the review [2]. The AFM zigzag state is shown in Fig. 3(a). The results are shown in Table III. We find that the AFM Neel state is favored for $MnPS_3$ and the AFM zigzag state is favored for $CoPS_3$ and

TABLE III. The calculated ground state magnetic orders, magnetic moments, and the band gaps for monolayer MPS_3 (M = Mn, Fe, Co, Ni) using GGA+U ($U_{\mathrm{eff}} = 0$ or 4 eV).

$U_{\mathrm{eff}} = 0$	Ground state magnetic order	Moment (μ_B)	Gap (eV)
$MnPS_3$	AFM Neel	4.23	1.32
$FePS_3$	AFM zigzag	3.30	0.02
$CoPS_3$	AFM zigzag	2.18	0.25
$NiPS_3$	AFM zigzag	1.08	0.71
$U_{\mathrm{eff}} = 4$ eV	Ground state magnetic order	Moment (μ_B)	Gap (eV)
$MnPS_3$	AFM Neel	4.52	2.27
$FePS_3$	AFM Neel	3.57	1.96
$CoPS_3$	AFM zigzag	2.58	1.83
$NiPS_3$	AFM zigzag	1.46	1.88

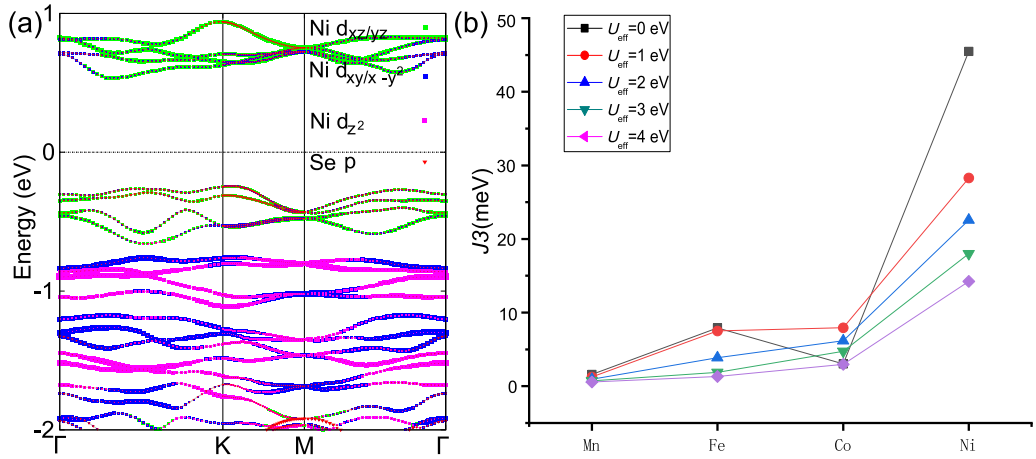

FIG. 7. (a) The band structure of $NiPS_3$ in the AFM zigzag state. (b) J_3 superexchange AFM interactions in MPS_3 (M = Mn, Fe, Co, Ni), which are extracted from the GGA+U calculations with the values $U_{\text{eff}} = (0, 1, 2, 3, 4)$ eV.

$NiPS_3$, which is generally consistent with the experimental results in bulk MPS_3 materials [6,32]. For $FePS_3$, the AFM zigzag state is favored when $U_{\text{eff}} < 2$ eV. Our DFT calculation can give the insulating states even without considering U_{eff}. With U_{eff} in GGA+U method, all four monolayer transition metal phosphorous trisulfides become AFM insulators, as shown in Table III. As a typical example, we plot the insulating band structure in the AFM zigzag state for $NiPS_3$ in Fig. 7(a). The Mn, Fe, Co, and Ni atoms are in high spin states and the magnetic moments slightly increase as U_{eff} increases. For bulk materials, the experimental band gaps are 3.0, 1.5, and 1.6 eV for Mn, Fe, and Ni-based compounds, respectively [2]. As shown in Table III, the calculated band gaps by GGA+U at $U_{\text{eff}} = 4$ eV are quantitatively close to the experimental values. Our calculated magnetic exchange parameters are also consistent with Wildes *et al.*'s experimental results [33–35]. For $NiPS_3$, the agreement can be quantitative. In our calculation, the J_1, J_2, and J_3 of $NiPS_3$ are -3.41, -0.22, and 14.24 meV with $U_{\text{eff}} = 4$ eV. In Lancon *et al.*'s experimental paper [35], the reported values are -1.9, 0.1, and 6.9 meV. However, the experimental values count each pair twice so that we need to divide the calculated values by a factor of 2 in order to compare with the experimental values, which results in a quantitative agreement.

The classical energies of the four different magnetic states for the effective Heisenberg model are given by

$$\begin{aligned} E_{\text{FM}} &= S^2(6J_1 + 12J_2 + 6J_3) + E_0, \\ E_{\text{AFM-Neel}} &= S^2(-6J_1 + 12J_2 - 6J_3) + E_0, \\ E_{\text{AFM-zigzag}} &= S^2(2J_1 - 4J_2 - 6J_3) + E_0, \\ E_{\text{AFM-stripy}} &= S^2(-2J_1 - 4J_2 + 6J_3) + E_0. \end{aligned} \tag{7}$$

From the calculated energies of these states, we can extract the effective magnetic exchange interactions. Those MPS_3 compounds are in the high-spin states, so we take the spin values to be the high spin of the atoms for simplicity. For example, the Ni^{2+} ion has two unpaired electrons, so the spin $S = 1$. The results are listed in Table IV. Some similar results have been obtained previously [13]. Our calculation are generally consistent with these previous calculations [13].

Here we pay special attention to the values in $NiPX_3$. As shown in Table IV, for $NiPX_3$, among the three magnetic exchange coupling parameters, J_3 is one order of magnitude larger than the other two parameters. Moreover, J_3 is strongly AFM while J_1 and J_2 both are weakly FM. These qualitative features are independent of U_{eff}. The dominance of J_3 over the other two further confirms the extracted physical picture of the weakly coupled four sublattices as shown in Fig. 3(b) based on the hopping parameters in the electronic band structure.

J_3 stems from so-called AFM super-superexchange interaction [6,31]. In Fig. 7(b) we plot the values of J_3 as a function of M (M = Mn, Fe, Co, Ni). In Fig. 7(b), it is clear that J_3 reaches the maximum value in $NiPX_3$, which can be easily understood as the hall-filling of e_g orbitals maximize the super-superexchange interaction.

V. THE TWO-ORBITAL *t*-*J* MODEL AND DOPING PHASE DIAGRAM FOR $NiPX_3$

From the above analysis and the known experimental facts [6], it is clear that $NiPX_3$ must belong to strongly correlated electron systems. The bandwidth of the two e_g orbitals is only

TABLE IV. The calculated exchange interaction parameters J_1, J_2, and J_3 for monolayer MPS_3 (M = Mn, Fe, Co, Ni) and $NiPSe_3$ using GGA+U ($U_{\text{eff}} = 0$ or 4 eV).

$U_{\text{eff}} = 0$	J_1 (meV)	J_2 (meV)	J_3 (meV)
$MnPS_3$	3.67	0.35	1.62
$FePS_3$	−15.65	1.17	7.93
$CoPS_3$	−17.41	9.92	3.04
$NiPS_3$	−5.52	−0.38	45.50
$NiPSe_3$	−9.26	−0.08	42.98
$U_{\text{eff}} = 4$ eV	J_1 (meV)	J_2 (meV)	J_3 (meV)
$MnPS_3$	1.39	0.09	0.56
$FePS_3$	1.39	0.15	1.32
$CoPS_3$	−0.47	−0.19	2.96
$NiPS_3$	−3.41	−0.22	14.24
$NiPSe_3$	−3.62	0.51	16.06

about 1 eV, much less than the band gaps in their AFM zigzag states. Moreover, as we showed above, the experimental band gaps are close to the theoretical results when we take $U_{\rm eff} \sim 4$ eV, which is much larger than the bandwidth as well. Thus, the magnetic order is caused by the strong electron-electron correlation.

Following the standard argument, $NiPX_3$, just like many other strongly correlated electron systems, must be a Mott insulator. As $U_{\rm eff}$ is much larger than the bandwidth, we can take the large U limit to derive a t-J type of model. For $NiPX_3$, a minimum two-orbital t-J model can be written as

$$H_{tJ} = \hat{P}H_0\hat{P} + \sum_{ij} H_{J,\langle ij\rangle}, \tag{8}$$

where $\hat{P}$ is the projection operator to remove the double occupancy and $H_{J,\langle ij\rangle}$ is the effective interaction. In a two-orbital model, in general, we should consider a spin-orbital Kugel-Khomskii type of superexchange interactions [36,37]. However, here, because the hopping is dominated by the TNN σ couplings, in the first order approximation, the leading interaction can be derived as

$$H_{J,\langle ij\rangle} = J_3\left(\mathbf{S}_{i,\bar{ij}} \cdot \mathbf{S}_{j,\bar{ij}} - \tfrac{1}{4}\mathbf{n}_{i,\bar{ij}}\mathbf{n}_{j,\bar{ij}}\right), \tag{9}$$

where $\langle ij\rangle$ is a TNN link, and $\mathbf{S}_{i,\bar{ij}}$ and $\mathbf{n}_{i,\bar{ij}}$ are the spin and density operators of the electron located at the orbital which participates σ hopping through the $\langle ij\rangle$ link at the ith site, respectively.

Before we present a full mean-field calculation for the above model, we would like to qualitatively argue possible superconducting states. By decoupling the J_3 AFM interaction in the pairing channel, the Bogoliubov–de Gennes (BdG) Hamiltonian in Nambu space $\Psi_k^\dagger = (\psi_{k\uparrow}^\dagger, \psi_{\bar{k}\downarrow}^T)$ for a uniform superconducting state can be generally written as

$$h_{Bk} = \begin{pmatrix} h_k & \Gamma_k \\ \Gamma_k^\dagger & -h_{\bar{k}}^T \end{pmatrix}, \quad \Gamma_k = \begin{pmatrix} 0 & \Delta_k \\ \Delta_{\bar{k}}^T & 0 \end{pmatrix}, \tag{10}$$

with $\bar{k} \equiv -k$ and h_k given in Eq. (2). Here the general form of pairing matrix is

$$\Delta_k = \sum_j e^{-i\mathbf{k}\cdot\mathbf{a}_{3j}}\Delta_j e^{il\theta_j}, \tag{11}$$

where θ_j is the angle of the TNN vector $\mathbf{a}_{3j}$, Δ_j is the two-orbital pairing matrix on bonds connected by $\mathbf{a}_{3j}$, and l is the angular momentum quantum number of the order parameter, with $(l = 0, \pm 2, \dots)$ representing $(s, d, \dots)$ waves in the singlet pairing channels.

If we only consider the σ bond hoppings, the electronic structure is identical to an isotropic one-orbital honeycomb model. In this case the real space pairing matrices reduce to a constant number $\Delta_j \sim \Delta_0$ and the true gap can be represented with $G(k) = \sqrt{\max(|\Delta_k|^2, |\Delta_{\bar{k}}|^2)}$. The Δ_k for the $d \pm id$ wave and the extended s wave can be explicitly written as

$$\Delta_k^s = \Delta_0[e^{2ik_y} + 2e^{-ik_y}\cos(\sqrt{3}k_x)], \tag{12}$$

$$\Delta_k^{d\pm id} = -\Delta_0\left[e^{2ik_y} + 2e^{-ik_y}\cos\left(\sqrt{3}k_x \pm \frac{2\pi}{3}\right)\right]. \tag{13}$$

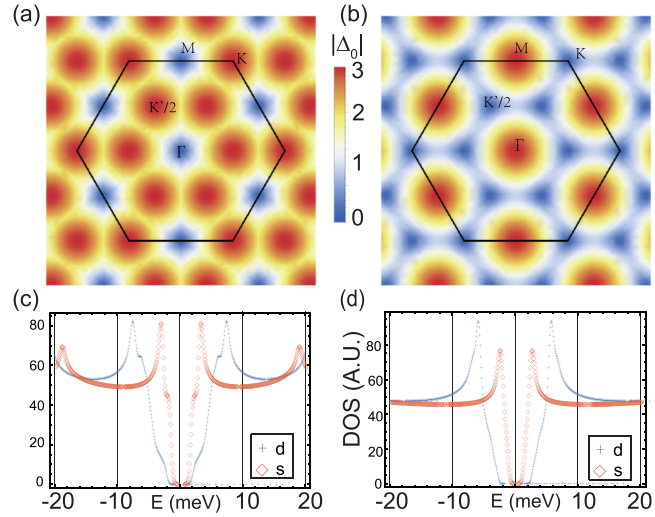

FIG. 8. (a) and (b) The amplitude distributions of the superconducting gap $G(k)$ of the $d \pm id$-wave and the extended s-wave states, respectively. (c) and (d) The density of states in the $d \pm id$-wave and the extended s-wave states at a doping level, $n = 3.8$ and 4.2, respectively, by taking $\Delta_0 = 0.3$ and $J_3 = 40$ meV.

In Figs. 8(a) and 8(b) we draw the one-orbital $d \pm id$ wave and the extended s wave gap distribution. The $d \pm id$ pairing gap peaks locate at $K(K')$ and $K(K')/2$ while the s pairing gap has peaks around Γ and M. At low doping, the Fermi surfaces are around $K(K')$ and $K(K')/2$ as seen from Fig. 2. Thus, following the general argument given in [14], known as the Hu-Ding principle, the $d \pm id$-wave pairing is favored over the s-wave pairing as the former would open a much bigger superconducting gap on the Fermi surfaces to save more energy than the latter.

Although the analytic formula for the gap cannot be obtained, this above analysis can be extended to the two-orbital model. In Figs. 8(c) and 8(d) we numerically calculate the density of states of the $d \pm id$-wave and s-wave superconducting states in the full two-orbital model by assuming the pairing amplitudes Δ_0 in both states are identical in all the σ bonds. It is clear that the $d \pm id$ state has much bigger superconducting gap than the s-wave state at low doping. Moreover, The s-wave pairing state can be gapless while the $d \pm id$ state has a full gap, which stems from the mismatch of the s-wave pairing momentum form factor with the normal state Fermi surfaces, the essential idea behind the Hu-Ding principle [14]. With a very large doping level, the Lifishitz transition of the Fermi surfaces merges pockets around M and Γ. As a result, the s-wave pairing can become highly competitive. However, in this region, the AFM fluctuation also becomes very weak so that the superconductivity likely vanishes.

Our slave-boson mean-field result on the pairing symmetry is consistent with the above analysis. Here we report the magnetic and superconducting phase diagram from the $U(1)$ slave-boson mean field for the model in Eq. (8) [38,39]. The method has been shown to provide correct qualitative information of the phase diagram as a function of doping. The slave-boson measures the electron occupancy and leads to the renormalization of hopping amplitude [40]. The detailed procedure is given in Appendix B. An illustration of the

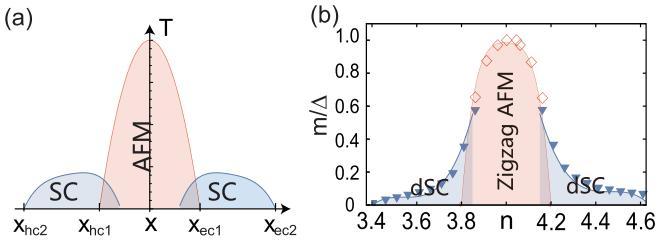

FIG. 9. The phase diagram under doping. (a) The sketch of a typical magnetism versus superconductivity phase diagram. (b) The zigzag magnetic order parameter and $d \pm id$ pairing strength as doping increases in the two-orbital model calculated by the slave-Boson mean field with $J_3 = 40$ meV. When the electrons per unit cell $n = 4.2$ ($x_{c1} = 0.1$), zigzag antiferromagnetic order parameter vanishes. As the doping increases, the superconductivity order parameter decreases and vanish around $n = 4.7$ ($x_{c2} = 0.35$). The hole doped phase diagram is almost symmetric for magnetic phase, while superconductivity vanished around $n = 3.4$ (0.3 hole doping).

phase diagram is sketched in Fig. 9(a) with the doping vs temperature. At low doping $x < x_{c1}$, the system would stay in antiferromagnetic state. Between two critical doping levels $x_{c1} < x < x_{c2}$, it is the superconducting phase. Near the quantum critical point, there might be coexistence of magnetism and superconductivity, or some other rich intertwined orders.

Our mean-field calculation results are plotted in Fig. 9(b). Here we adopt $J_3 = 40$ meV $\sim t^{\mathrm{TNN}}_{yzyz}/6$. The density $n = 4$ represents half-filling and the doping level of x electron per Ni atom corresponds to $n = 4 + 2x$. Owing to the orbital selective exchange, the long-range AFM zigzag order vanishes around the doping level of 0.1 electron per Ni atom ($n = 4.2$) away from half-filling. If we take $J_3 = 80$ meV, this critical doping value increases 0.2 per Ni atom ($n = 4.4$), which is similar to the mean-field result in cuprates [38] by the same method. Superconducting order parameters also decreases as doping increase. When the doping reaches 0.35 per Ni atom ($n = 4.7$), the superconducting order parameter Δ_0 becomes too small to have any physical meaning. In all these doping region with superconductivity, $d \pm id$-wave pairing is energetically favorable over the extended s wave. It is worth mentioning that the phase diagram is slightly asymmetric between the hole and electron doped region. The magnetism is almost symmetric, vanishing around $x_{c1} \approx \pm 0.1$, and the superconductivity decreases slightly faster with hole doping.

VI. DISCUSSION

In summary, we have shown that the Ni-based TMTs are close to a strongly correlated quadruple-layer graphene and are Dirac materials described by a two-orbital model with the strong electron-electron interaction. The main electronic kinematics and magnetic interactions exist with unusual long-range distance between two third nearest-neighbor Ni atoms, which stems from the super-superexchange mechanism. With this underlining electronic structure, the materials provide a simple and ideal playground to investigate strong correlation physics.

The two-orbital model can be viewed as a natural extension of the single orbital model in the conventional high temperature superconductors, cuprates. Recently, materials with both active e_g orbitals have gained much attention. $Ba_2CuO_{3+\delta}$ [41], synthesized under high pressure, is likely an extremely heavy hole doped cuprate. As the Jahn-Teller distortion of the CuO_6 octahedron causes a shorter Cu-O bond along the c axis than the in-plane ones, both e_g orbitals become important [42]. The single CuO_2 layer grown by MBE also has a similar electronic structure [43]. In $La_2Ni_2Se_2O_3$, a recent theoretically proposed candidate of Ni-based high temperature superconductors [44], the low energy physics is also attributed to the two e_g orbitals of Ni atoms. If the superconductivity is determined to arise in the two-orbital model, the Ni-based TMTs, together with these materials, can provide us much needed information to solve the elusive mechanism of high temperature superconductivity.

Comparing with recent artificial graphene systems, in which new bands are created to reduce the kinetic energy so that the effect of the weak electron-electron correlation can arise in the standard graphene [12], the Ni-based TMTs are simply in the other limit (Mott limit) with the strong electron-electron correlation. We can consider to increase the kinetic energy, namely the bandwidth, to enter the Mott transition critical region. In general, the bandwidth can be increased by applying pressure or by atom substitutions. During these processes, the angles between Ni-S/Se-Ni can be changed greatly as well, which can lead to different intriguing physics. For example, in this case, more spin-orbital superexchange interaction terms may be important, which can lead to exciting interplay between orbital and spin degrees of freedom.

Experimentally, MPX_3 compounds have been doped with charge carriers, especially via intercalation by lithium, as they were candidates for battery materials [45,46]. However, intercalation is essentially a bulk process and may not be easily applied to the exfoliated monolayers that are considered here. Recently, modern gating technology can induce carriers to a variety of two-dimensional materials [47]. The monolayer Ni-based TMTs can be an important playground for this modern technology.

ACKNOWLEDGMENTS

We thank Hong Jiang, Xinzheng Li, Xianxin Wu, Yuechao Wang, Shengshan Qin, and Dong Luan for useful discussion. The work is supported by the Ministry of Science and Technology of China 973 program (Grants No. 2015CB921300, No. 2017YFA0303100, and No. 2017YFA0302900), National Science Foundation of China (Grant No. NSFC-11334012), the Strategic Priority Research Program of CAS (Grant No. XDB07000000), and High-performance Computing Platform of Peking University. Yuhao Gu especially thanks Hong Jiang for his kind supervision and detailed teaching. Qiang Zhang acknowledges the support from the International Young Scientist Fellowship of Institute of Physics CAS (Grant No. 2017002) and the Postdoctoral International Program (2017) from China Postdoctoral Science Foundation.

APPENDIX A: THE EXPLICIT FORM OF EFFECTIVE HAMILTONIAN

The tight-binding effective Hamiltonian H_0 in Eq. (1) is a 4×4 matrix. The explicit form of its elements is given by

$$
\begin{aligned}
H_{11} &= t^{\mathrm{SNN}}_{xzxz}\left(2\cos k_x+\cos\frac{k_x}{2}\cos\frac{\sqrt{3}k_y}{2}\right)+3t^{\mathrm{SNN}}_{yzyz}\cos\frac{k_x}{2}\cos\frac{\sqrt{3}k_y}{2},\\
H_{12} &= t^{\mathrm{SNN}}_{xzxz}\left(-\sqrt{3}\sin\frac{k_x}{2}\sin\frac{\sqrt{3}k_y}{2}\right)+t^{\mathrm{SNN}}_{yzyz}\left(\sqrt{3}\sin\frac{k_x}{2}\sin\frac{\sqrt{3}k_y}{2}\right)+i\left[4t^{\mathrm{SNN}}_{xzyz}\sin\frac{k_x}{2}\left(\cos\frac{k_x}{2}-\cos\frac{\sqrt{3}k_y}{2}\right)\right],\\
H_{13} &= \frac{1}{2}\left(\left(t^{\mathrm{NN}}_{xzxz}+3t^{\mathrm{NN}}_{yzyz}\right)\cos\frac{k_x}{2}\cos\frac{k_y}{2\sqrt{3}}+\left[2t^{\mathrm{NN}}_{xzxz}+\left(t^{\mathrm{TNN}}_{xzxz}+3t^{\mathrm{TNN}}_{yzyz}\right)\cos k_x\right]\cos\frac{k_y}{\sqrt{3}}+2t^{\mathrm{TNN}}_{xzxz}\cos\frac{2k_y}{\sqrt{3}}\right)\\
&\quad-\frac{i}{2}\left\{\left(3t^{\mathrm{NN}}_{xzxz}+t^{\mathrm{NN}}_{yzyz}\right)\cos\frac{k_x}{2}-2\cos\frac{k_y}{2\sqrt{3}}\left[\left(3t^{\mathrm{TNN}}_{xzxz}+t^{\mathrm{TNN}}_{yzyz}\right)\cos k_x+2\left(2t^{\mathrm{NN}}_{yzyz}-2t^{\mathrm{TNN}}_{yzyz}\cos\frac{k_y}{\sqrt{3}}\right)\right]\right\}\sin\frac{k_y}{2\sqrt{3}},\\
&\quad-\frac{i}{2}\left\{\left(t^{\mathrm{NN}}_{xzxz}+3t^{\mathrm{NN}}_{yzyz}\right)\cos\frac{k_x}{2}-2\cos\frac{k_y}{2\sqrt{3}}\left[\left(t^{\mathrm{TNN}}_{xzxz}+3t^{\mathrm{TNN}}_{yzyz}\right)\cos k_x+2\left(t^{\mathrm{NN}}_{xzxz}-2t^{\mathrm{TNN}}_{xzxz}\cos\frac{k_y}{\sqrt{3}}\right)\right]\right\}\sin\frac{k_y}{2\sqrt{3}},\\
H_{14} &= \frac{\sqrt{3}}{2}\left(\left(t^{\mathrm{NN}}_{xzxz}-t^{\mathrm{NN}}_{yzyz}\right)\sin\frac{k_x}{2}\sin\frac{k_y}{2\sqrt{3}}+\left(t^{\mathrm{TNN}}_{xzxz}-t^{\mathrm{TNN}}_{yzyz}\right)\sin k_x\sin\frac{k_y}{\sqrt{3}}\right)\\
&\quad+\frac{\sqrt{3}i}{2}\left(\left(t^{\mathrm{NN}}_{xzxz}-t^{\mathrm{NN}}_{yzyz}\right)\cos\frac{k_y}{2\sqrt{3}}+2\left(t^{\mathrm{TNN}}_{yzyz}-t^{\mathrm{TNN}}_{xzxz}\right)\cos\frac{k_x}{2}\cos\frac{k_y}{\sqrt{3}}\right)\sin\frac{k_x}{2},\\
H_{22} &= t^{\mathrm{SNN}}_{yzyz}\left(2\cos k_x+\cos\frac{k_x}{2}\cos\frac{\sqrt{3}k_y}{2}\right)+3t^{\mathrm{SNN}}_{xzxz}\cos\frac{k_x}{2}\cos\frac{\sqrt{3}k_y}{2},\\
H_{24} &= \frac{1}{2}\left(\left(3t^{\mathrm{NN}}_{xzxz}+t^{\mathrm{NN}}_{yzyz}\right)\cos\frac{k_x}{2}\cos\frac{k_y}{2\sqrt{3}}+\left[2t^{\mathrm{NN}}_{yzyz}+\left(3t^{\mathrm{TNN}}_{xzxz}+t^{\mathrm{TNN}}_{yzyz}\right)\cos k_x\right]\cos\frac{k_y}{\sqrt{3}}+2t^{\mathrm{TNN}}_{yzyz}\cos\frac{2k_y}{\sqrt{3}}\right)\\
&\quad-\frac{i}{2}\left[\left(3t^{NN}_{xzxz}+t^{NN}_{yzyz}\right)\cos\frac{k_x}{2}-2\cos\frac{k_y}{2\sqrt{3}}\left(\left(3t^{\mathrm{TNN}}_{xzxz}+t^{\mathrm{TNN}}_{yzyz}\right)\cos k_x+2\left(t^{\mathrm{NN}}_{yzyz}-2t^{\mathrm{TNN}}_{yzyz}\cos\frac{k_y}{\sqrt{3}}\right)\right)\right]\sin\frac{k_y}{2\sqrt{3}},
\end{aligned}
\tag{A1}
$$

with $H_{23}=H_{14}, H_{33}=H_{11}, H_{34}=H^*_{12}$ and $H_{44}=H_{22}$ by symmetry. These hopping parameters are given in Table II in the main text.

APPENDIX B: FORMULATION OF THE SLAVE-BOSON MEAN FIELD

We provide the detailed procedure for the slave-boson mean-field method on the Hamiltonian Eq. (8). In our two-orbital model, the two e_g orbitals are degenerate so that they have the identical occupancy. In the slave-boson approximation [40], the same occupancy for all the orbitals leads to the same renormalization for all the hopping interaction. Namely, we have

$$\hat{P}H_0\hat{P}=\left|\frac{n}{4}-1\right|H_0, \tag{B1}$$

in which $n=4\pm2x$, x is the doped electron (+) or hole (−) per atom. $n=4$ represents the half-filling, where the kinetic energy vanishes and the Hamiltonian reduces to pure Heisenberg exchange interaction. The exchange term $H_{J,\langle ij\rangle}$ in Eq. (8) can be decoupled into superconducting and magnetic channels.

In the superconducting channel, it is

$$-\frac{J_3}{2}\sum_{ij}(\langle\Delta^\dagger_{ij}\rangle\Delta_{ij}+\Delta^\dagger_{ij}\langle\Delta_{ij}\rangle)+E_s, \tag{B2}$$

with pairing matrix $\Delta^\dagger_{ij}\equiv\sigma a^\dagger_{i\bar{i}j,\sigma}a^\dagger_{j\bar{i}j,\bar{\sigma}}$ with $a_{i\bar{i}j,\sigma}=\cos\theta_{ij}a_{ix,\sigma}+\sin\theta_{ij}a_{iy,\sigma}$ and the constant part

$$E_s=\frac{J_3}{2}\sum_{ij}(\langle\Delta^\dagger_{ij}\rangle\langle\Delta_{ij}\rangle+n_{i\bar{i}j,\sigma}n_{j\bar{i}j,\sigma}), \tag{B3}$$

with the spin indices $\bar{\sigma}=-\sigma=\pm1$ and link ij the TNN bond. The same spin coupling density term $n_{i\bar{i}j,\sigma}n_{j\bar{i}j,\sigma}$ term in E_s would be decoupled as bond hopping $\langle a^\dagger_{i\bar{i}j,\sigma}a_{j\bar{i}j,\sigma}\rangle a_{i\bar{i}j,\sigma}a^\dagger_{j\bar{i}j,\sigma}$ according to the approach in literature [38]. Those bond hopping terms effectively renormalize the third neighbor σ-bond hoppings to affect the position and shape of Fermi surface. The hopping parameters and Fermi surfaces will be renormalized as the doping varies in our model. Thus as a simple illustrating of the phase diagram under slave-boson method, those bond hopping terms would be simply taken as the density correlation. Put the renormalized hopping and decoupled exchange terms together, in the two-orbital momentum space, we obtain $\sum_k\Psi^\dagger_k h_{Bk}\Psi_k+E_s$ with h_{Bk} given in Eq. (10).

In the magnetic channel, the J_3 dominated spin exchange interaction prefers the zigzag AFM state as shown in Fig. 3. In the mean-field level, the magnetic order in the zigzag pattern is given by $\langle\mathbf{S}_i\rangle=(-1)^{i_2}m_0\hat{z}$ with $\mathbf{i}=i_1\mathbf{a_2}_1+i_2\mathbf{a_2}_2$. It is important to point out that as only the σ bond orbitals are considered, the spin exchange is orbital selective. That is to

say, the spin operator $\mathbf{S}_{i,\bar{i}j} = \frac{1}{2} a^{+}_{i\bar{i}j\mu} \boldsymbol{\sigma}_{\mu\nu} a_{i\bar{i}jv}$ with $\boldsymbol{\sigma}$ the vector of three Pauli matrices. As a result

$$\langle S^z_{i,\bar{i}j} \rangle = \cos^2\theta_{\bar{i}j} m_{ixx} + \sin^2\theta_{\bar{i}j} m_{iyy} + \cos\theta_{\bar{i}j} \sin\theta_{\bar{i}j} (m_{ixy} + m_{iyx}), \tag{B4}$$

with $m_{i\alpha\beta} \equiv \langle \sigma (a^{\dagger}_{i\alpha\sigma} a_{i\beta\sigma}) \rangle / 2 = (-1)^{i_2} m_{\alpha\beta}$. Up to a constant term, $H_{J,\langle ij \rangle}$ is decoupled as

$$\sum H_{J,\langle ij \rangle} = \sum_k \sigma a^{\dagger}_{k\alpha\sigma} M_{2\alpha\beta} a_{k+Q_1\beta\sigma}, \tag{B5}$$

with $\mathbf{Q}_1 = \mathbf{G}_2/2$ marked in Fig. 5 as the ordered magnetic wave vector. The scattering matrix from $\mathbf{k}$ to $\mathbf{k} + \mathbf{Q_1}$ in e_g orbitals space is

$$M_2 = -\frac{3J_3}{16} \begin{pmatrix} 3m_{xx} + m_{yy} & m_{xy} + m_{yx} \\ m_{xy} + m_{yx} & m_{xx} + 3m_{yy} \end{pmatrix}. \tag{B6}$$

Defining $\Psi^{\dagger}_{Mk} = (\Psi^{\dagger}_k, \Psi^{\dagger}_{k+Q_1})$, the mean-field Hamiltonian can be written as

$$H = \sum_{k \in \mathrm{rBZ}} (\Psi^{\dagger}_M A_k \Psi_{Mk} + \mathrm{tr}(h_k + h_{k+Q_1}) - 8\mu) + E_{sm}, \tag{B7}$$

with rBZ representing the reduced Brillouin zone due to the magnetic cell and A_k is a 16×16 matrix as

$$A_k = \begin{pmatrix} h_{Bk} & I_2 \bigotimes I_2 \bigotimes M_2 \\ I_2 \bigotimes I_2 \bigotimes M_2^{\dagger} & h_{Bk+Q} \end{pmatrix}, \tag{B8}$$

$$\frac{E_{sm}}{N} = \frac{3J_3}{2} \Delta_0^2 + \frac{3J_3}{8} \left[3m_{xx}^2 + 3m_{yy}^2 + 2m_{xx} m_{yy} + (m_{xy} + m_{yx})^2 + n^2 \right]. \tag{B9}$$

In A_k, the first I_2 is for particle-hole space and the second is for A-B sublattice. The h_{Bk} is given in Eq. (10). The self-consistency of the chemical potential is also taken into consideration for a fixed doping. It is easy to show that

$$\begin{aligned} n_k + n_{k+Q_1} &= 8 + \mathrm{tr}(\Sigma \langle \Psi_{Mk} \Psi^{\dagger}_{Mk} \rangle) \\ &= 8 - \mathrm{tr}[\Sigma U_k f(\Lambda_k) U_k^{\dagger}], \end{aligned} \tag{B10}$$

in which Σ is the 16×16 stagger matrix $\Sigma \equiv -I_2 \bigotimes \sigma_3 \bigotimes I_4$, $U_k^{\dagger} A_k U_k = \Lambda_k$, diagonalizes the A_k, and $f(\Lambda_k)$ is the Fermi distribution function.

It is worth mentioning that the numerical result indicates slight difference between the intraorbital magnetic orders m_{xx} and m_{yy} due to the rotation symmetry breaking in the AFM zigzag state. The interorbital magnetic orders m_{xy} and m_{yx} are very small and can be ignored in the mean-field solution.

[1] K. S. Novoselov, A. K. Geim, S. V. Morozov, D. Jiang, Y. Zhang, S. V. Dubonos, I. V. Grigorieva, and A. A. Firsov, Electric field effect in atomically thin carbon films, Science **306**, 666 (2004).

[2] F. Wang, A. Shifa Tofik, P. Yu, P. He, Y. Liu, F. Wang, Z. Wang, X. Zhan, X. Lou, F. Xia, and J. He, Frontiers on van der Waals layered metal phosphorous trichalcogenides, Adv. Funct. Mater. **28**, 1802151 (2018).

[3] M. A. Susner, M. Chyasnavichyus, M. A. McGuire, P. Ganesh, and P. Maksymovych, Metal thio- and selenophosphates as multifunctional van der Waals layered materials, Adv. Mater. **29**, 1602852 (2017).

[4] C. Friedel, Sur une nouvelle série de sulfophosphures, les thiohypophosphates, Compt. Rend. **119**, 260 (1894).

[5] L. Ferrand, Bull. Soc. Chim. **13**, 115 (1895).

[6] G. Le Flem, R. Brec, G. Ouvard, A. Louisy, and P. Segransan, Magnetic interactions in the layer compounds MPX_3 (M = Mn, Fe, Ni; X= X, Se), J. Phys. Chem. Solids **43**, 455 (1982).

[7] Y. Wang, J. Ying, Z. Zhou, J. Sun, T. Wen, Y. Zhou, N. Li, Q. Zhang, F. Han, Y. Xiao *et al.*, Emergent superconductivity in an iron-based honeycomb lattice initiated by pressure-driven spin-crossover, Nat. Commun. **9**, 1914 (2018).

[8] S. Y. Kim, T. Y. Kim, L. J. Sandilands, S. Sinn, M.-C. Lee, J. Son, S. Lee, K.-Y. Choi, W. Kim, B.-G. Park, C. Jeon, H.-D. Kim, C.-H. Park, J.-G. Park, S. J. Moon, and T. W. Noh, Charge-Spin Correlation in van der Waals Antiferromagnet $NiPS_3$, Phys. Rev. Lett. **120**, 136402 (2018).

[9] Y. Sugita, T. Miyake, and Y. Motome, Multiple Dirac cones and topological magnetism in honeycomb-monolayer transition metal trichalcogenides, Phys. Rev. B **97**, 035125 (2018).

[10] C. Wu, D. Bergman, L. Balents, and S. Das Sarma, Flat Bands and Wigner Crystallization in the Honeycomb Optical Lattice, Phys. Rev. Lett. **99**, 070401 (2007).

[11] C. Wu and S. Das Sarma, $p_{x,y}$-orbital counterpart of graphene: Cold atoms in the honeycomb optical lattice, Phys. Rev. B **77**, 235107 (2008).

[12] Y. Cao, V. Fatemi, A. Demir, S. Fang, S. L. Tomarken, J. Y. Luo, J. D. Sanchez-Yamagishi, K. Watanabe, T. Taniguchi, E. Kaxiras *et al.*, Correlated insulator behaviour at half-filling in magic-angle graphene superlattices, Nature (London) **556**, 80 (2018).

[13] B. L. Chittari, Y. Park, D. Lee, M. Han, A. H. MacDonald, E. Hwang, and J. Jung, Electronic and magnetic properties of single-layer MPX_3 metal phosphorous trichalcogenides, Phys. Rev. B **94**, 184428 (2016).

[14] J. Hu and H. Ding, Local antiferromagnetic exchange and collaborative Fermi surface as key ingredients of high temperature superconductors, Sci. Rep. **2**, 381 (2012).

[15] J. Hu, Identifying the genes of unconventional high temperature superconductors, Sci. Bull. **61**, 561 (2016).

[16] K. Seo, B. A. Bernevig, and J. Hu, Pairing Symmetry in a Two-Orbital Exchange Coupling Model of Oxypnictides, Phys. Rev. Lett. **101**, 206404 (2008).

[17] S. Lebegue and O. Eriksson, Electronic structure of two-dimensional crystals from *ab initio* theory, Phys. Rev. B **79**, 115409 (2009).

[18] J.-U. Lee, S. Lee, J. H. Ryoo, S. Kang, T. Y. Kim, P. Kim, C.-H. Park, J.-G. Park, and H. Cheong, Ising-type magnetic ordering in atomically thin $FePS_3$, Nano Lett. **16**, 7433 (2016).

[19] G. Ouvrard, R. Brec, and J. Rouxel, Structural determination of some MPS_3 layered phases (M= Mn, Fe, Co, Ni and Cd), Mater. Res. Bull. **20**, 1181 (1985).

[20] W. Klingen, G. Eulenberger, and H. Hahn, Über hexathio-und hexaselenohypodiphosphate vom typ $M^{II}_2P_2X_6$, Naturwissenschaften **55**, 229 (1968).

[21] R. R. Rao and A. Raychaudhuri, Magnetic studies of a mixed antiferromagnetic system $Fe_{1-x}Ni_xPS_3$, J. Phys. Chem. Solids **53**, 577 (1992).

[22] R. Brec, G. Ouvrard, A. Louisy, and J. Rouxel, Proprietes structurales de phases M(II)PX_3 (X= S, Se), Ann. Chim. Sci. Matér., 499 (1980).

[23] G. Kresse and J. Furthmüller, Efficiency of ab-initio total energy calculations for metals and semiconductors using a plane-wave basis set, Comput. Mater. Sci. **6**, 15 (1996).

[24] G. Kresse and D. Joubert, From ultrasoft pseudopotentials to the projector augmented-wave method, Phys. Rev. B **59**, 1758 (1999).

[25] J. P. Perdew, K. Burke, and M. Ernzerhof, Generalized Gradient Approximation made Simple, Phys. Rev. Lett. **77**, 3865 (1996).

[26] A. A. Mostofi, J. R. Yates, Y.-S. Lee, I. Souza, D. Vanderbilt, and N. Marzari, Wannier90: A tool for obtaining maximally-localised Wannier functions, Comput. Phys. Commun. **178**, 685 (2008).

[27] A. I. Liechtenstein, V. I. Anisimov, and J. Zaanen, Density-functional theory and strong interactions: Orbital ordering in Mott-Hubbard insulators, Phys. Rev. B **52**, R5467 (1995).

[28] Y. Li, X. Han, S. Qin, C. Le, Q.-H. Wang, and J. Hu, Robust d-wave pairing symmetry in multiorbital cobalt high-temperature superconductors, Phys. Rev. B **96**, 024506 (2017).

[29] D. J. Scalapino, A common thread: The pairing interaction for unconventional superconductors, Rev. Mod. Phys. **84**, 1383 (2012).

[30] H. Yao and F. Yang, Topological odd-parity superconductivity at type-II two-dimensional van Hove singularities, Phys. Rev. B **92**, 035132 (2015).

[31] A. R. Wildes, V. Simonet, E. Ressouche, G. J. McIntyre, M. Avdeev, E. Suard, S. A. J. Kimber, D. Lançon, G. Pepe, B. Moubaraki, and T. J. Hicks, Magnetic structure of the quasi-two-dimensional antiferromagnet $NiPS_3$, Phys. Rev. B **92**, 224408 (2015).

[32] A. R. Wildes, V. Simonet, E. Ressouche, R. Ballou, and G. J. McIntyre, The magnetic properties and structure of the quasi-two-dimensional antiferromagnet $CoPS_3$, J. Phys.: Condens. Matter **29**, 455801 (2017).

[33] A. R. Wildes, B. Roessli, B. Lebech, and K. W. Godfrey, Spin waves and the critical behaviour of the magnetization in $MnPS_3$, J. Phys.: Condens. Matter **10**, 6417 (1998).

[34] A. R. Wildes, K. C. Rule, R. I. Bewley, M. Enderle, and T. J. Hicks, The magnon dynamics and spin exchange parameters of $FePS_3$, J. Phys.: Condens. Matter **24**, 416004 (2012).

[35] D. Lançon, R. A. Ewings, T. Guidi, F. Formisano, and A. R. Wildes, Magnetic exchange parameters and anisotropy of the quasi-two-dimensional antiferromagnet $NiPS_3$, Phys. Rev. B **98**, 134414 (2018).

[36] C. Castellani, C. R. Natoli, and J. Ranninger, Magnetic structure of V_2O_3 in the insulating phase, Phys. Rev. B **18**, 4945 (1978).

[37] K. Kugel and D. Khomskii, The Jahn-Teller effect and magnetism: Transition metal compounds, Phys. Usp. **25**, 231 (1982).

[38] Q.-H. Wang, D.-H. Lee, and P. A. Lee, Doped t-J model on a triangular lattice: Possible application to $Na_xCoO_2 \cdot yH_2O$ and $Na_{1-x}TiO_2$, Phys. Rev. B **69**, 092504 (2004).

[39] J. Brinckmann and P. A. Lee, Renormalized mean-field theory of neutron scattering in cuprate superconductors, Phys. Rev. B **65**, 014502 (2001).

[40] A. Rüegg, M. Indergand, S. Pilgram, and M. Sigrist, Slave-boson mean-field theory of the Mott transition in the two-band Hubbard model, Eur. Phys. J. B **48**, 55 (2005).

[41] W. M. Li, J. F. Zhao, L. P. Cao, Z. Hu, Q. Z. Huang, X. C. Wang, Y. Liu, G. Q. Zhao, J. Zhang, Q. Q. Liu *et al.*, Superconductivity in a unique type of copper oxide, Proc. Natl. Acad. Sci. USA, **116**, 12156 (2019).

[42] T. A. Maier, T. Berlijn, and D. J. Scalapino, Two pairing domes as Cu^{2+} varies to Cu^{3+}, Phys. Rev. B **99**, 224515 (2019).

[43] K. Jiang, X. Wu, J. Hu, and Z. Wang, Nodeless High-T_c Superconductivity in Highly Overdoped Monolayer CuO_2, Phys. Rev. Lett. **121**, 227002 (2018).

[44] C. Le, J. Zeng, Y. Gu, G.-H. Cao, and J. Hu, A possible family of Ni-based high temperature superconductors, Sci. Bull. **63**, 957 (2018).

[45] R. Brec, Review on structural and chemical properties of transition metal phosphorous trisulfides MPS_3, Solid State Ionics **22**, 3 (1986).

[46] V. Grasso and L. Silipigni, Low-dimensional materials: The MPX_3 family, physical features and potential future applications, Riv. Nuovo Cimento **25**, 1 (2002).

[47] J. T. Ye, S. Inoue, K. Kobayashi, Y. Kasahara, H. T. Yuan, H. Shimotani, and Y. Iwasa, Liquid-gated interface superconductivity on an atomically flat film, Nat. Mater. **9**, 125 (2009).